Wang, H. Q.; Watkins, J. G.; Guo, H. Y.; Groth, M.; Jarvinen, A. E.; Leonard, A. W.; Ren, J.; Thomas, D. M.; Boedo, J.

Effects of divertor electrical drifts on particle distribution and detachment near the divertor target plate in DIII-D

Published in:
Physics of Plasmas

DOI:
10.1063/5.0048609

Published: 01/05/2021

Document Version
Publisher's PDF, also known as Version of record

Please cite the original version:
Wang, H. Q., Watkins, J. G., Guo, H. Y., Groth, M., Jarvinen, A. E., Leonard, A. W., Ren, J., Thomas, D. M., & Boedo, J. (2021). Effects of divertor electrical drifts on particle distribution and detachment near the divertor target plate in DIII-D. *Physics of Plasmas*, *28*(5), Article 052509. https://doi.org/10.1063/5.0048609

Physics of Plasmas ARTICLE scitation.org/journal/php

Effects of divertor electrical drifts on particle distribution and detachment near the divertor target plate in DIII-D

Cite as: Phys. Plasmas **28**, 052509 (2021); doi: 10.1063/5.0048609
Submitted: 24 February 2021 · Accepted: 26 April 2021 ·
Published Online: 18 May 2021

View Online Export Citation CrossMark

H. Q. Wang,[1,a)] J. G. Watkins,[2] H. Y. Guo,[1] M. Groth,[3] A. E. Jarvinen,[4] A. W. Leonard,[1] J. Ren,[5] D. M. Thomas,[1] and J. Boedo[6]

AFFILIATIONS

[1]General Atomics, P.O. Box 85608, San Diego, California 92186-5608, USA
[2]Sandia National Laboratories, P.O. Box 969, Livermore, California 94551, USA
[3]Aalto University, P.O. Box 11000, Aalto, Espoo FI-00076, Finland
[4]Lawrence Livermore National Laboratory, P.O. Box 808, Livermore, California 94550, USA
[5]University of Tennessee, Knoxville, Knoxville, Tennessee 37996-1410, USA
[6]University of California, San Diego, 9500 Gilman Dr., La Jolla, San Diego, California 92093, USA

[a)]Author to whom correspondence should be addressed: wanghuiqian@fusion.gat.com

ABSTRACT

Strong impacts of drifts on the divertor plasma in–out asymmetry and detachment are demonstrated in DIII-D with an open divertor configuration. For forward toroidal field, B_T, i.e., with the ion $B \times \nabla B$ drift toward the divertor, the particle flux to the inner divertor, as represented by the Langmuir probe measured ion saturation current (J_{sat}), exhibits a double peak structure, with electron temperature, lower at the inner target. Reversing the B_T direction reverses both the radial and poloidal $E \times B$ flows, leading to a broad particle flux profile in the outboard scrape-off layer (SOL) with a similar double-peak structure to that observed at the inner target with forward B_T. The correlation of a double peak structure with divertor temperature profiles confirms physical coupling between the drift flow and sheath boundary condition and their strong impact on divertor profiles. In addition, under reversed B_T conditions, increasing the density flattens the target temperature profile. However, J_{sat} remains high away from the strike point, rendering it difficult to achieve an "effective" detached plasma, i.e., with effective reduction in both peak heat flux and peak temperature (in the far SOL). In contrast, divertor detachment with a cold and flat temperature profile can be achieved at both target plates with the forward B_T.

I. INTRODUCTION

Understanding particle and heat transport to the divertor target plate is one of the most important issues for the operation of reactor-size devices, such as ITER.[1] Future machines, like ITER and DEMO, with higher power density requires significant reductions of both the heat and particle fluxes depositing at the target plate to not exceed the material limitations. The peaks of fluxes are the key parameters for the control of divertor plasmas, while the extent of the profiles is also crucially important for the power dissipation. Divertor design requires optimized control of divertor particle and heat profiles. In addition, the divertor conditions, i.e., density, temperature, particle, and heat profiles, could strongly influence the divertor recycling and neutral dynamics and thus affect the upstream plasmas, i.e., boundary plasma fueling and H-mode pedestal structures. However, the underlying physics mechanisms that determine the particle and heat distribution in the divertor or scrape-off layer (SOL) are not yet fully understood.

It is expected that the parallel transport along the magnetic field lines in the SOL/divertor region with open flux surfaces is much faster than the cross field transport, while the cross field transport is required to distribute the particle and energy to a wide region near the target plates. Based on the two-point model,[2] the divertor plasma condition strongly correlates with upstream plasmas. In turn, divertor plasma conditions could significantly affect the upstream–downstream relationship.[3]

Besides the upstream–downstream relationship, several other mechanisms are considered to influence the divertor plasma heat and particle profiles, such as the anomalous cross field transport, diamagnetic drift, $E \times B$ drift, plasma rotations, and ballooning-like transport.[4,5] Among them, it has been found that the $E \times B$ drift may play an important role in the plasma transport. For instance, recent numerical calculations suggest that the $E \times B$ drift can be the primary mechanism in the divertor in–out asymmetry, in agreement with experimental observations and theoretical predictions.[6–8] In this paper, we will focus on how divertor electrical drift flow affects the particle and power distributions near the divertor target plates.

The drift flow picture can be summarized as follows. In the favorable B_T direction, with ion $B \times \nabla B$ toward the divertor, the temperature gradient between the upstream and target plate and thus the resulting potential gradient drive radial $E \times B$ flux from the outboard SOL across the separatrix into the private flux region. Near the inboard strike point, such radial $E \times B$ drift moves the particles from the private flux region to inboard SOL. In addition, the radial gradient of plasma potential and thus the radial electric field drive the poloidal $E \times B$ particle flux from the outboard private flux along the poloidal magnetic field toward the inboard strike point. Reversing the B_T does not significantly change the electric field direction but does change the drift direction, which can reduce or even reverse the in–out asymmetry. It should be pointed out that the amplitude of potential gradient and thus the electric field strongly depend on the divertor conditions; for example, in the hot divertor with high temperature near the divertor target, the poloidal drift in the divertor would be the dominant flow, while in the cold divertor, the poloidal drift is reduced with low temperature, but the radial drift is enhanced. Such a competition between different drifts would strongly affect the divertor particle and heat flux profiles.

Even at a local divertor region, the drift could strongly affect the profiles, such as forming the double-peak structures. With a double peak structure, the SOL profiles cannot be described by the exponential-like functions which have been commonly used in many experimental and simulation studies.[9] Such profiles with double peak structure have been observed in many machines.[3,10–13] In this paper, we will highlight that the double peak structure is mainly due to the important transport effects taking place in the divertor.

In this paper, we will introduce the experimental measurements of divertor potential and radial electric field at the target plate. Most of the data are taken from the divertor Langmuir probe system, which is currently equipped by most of the tokamak devices all over the world. Then we compare the target profiles, including the particle, heat flux, potential, and drift in different divertor conditions and with different B_T directions. A double-peak structure appears at the inboard SOL in favorable B_T plasmas and is shifted to the outboard SOL in reversed B_T plasmas. With increasing density approaching detachment, the double-peak structure disappears, which is consistent with the divertor drift picture. We will discuss the possible physical mechanisms for the double peak structure.

II. DIAGNOSTICS AND EXPERIMENTAL SETUP

These investigations were carried out in the DIII-D tokamak in a lower single null divertor configuration with the outer strike point on the horizontal target plate and inner strike point on a slanted target plate (Fig. 1). The target profiles are obtained from a fixed radial Langmuir probe array embedded in the divertor plate.[14] An adjustable

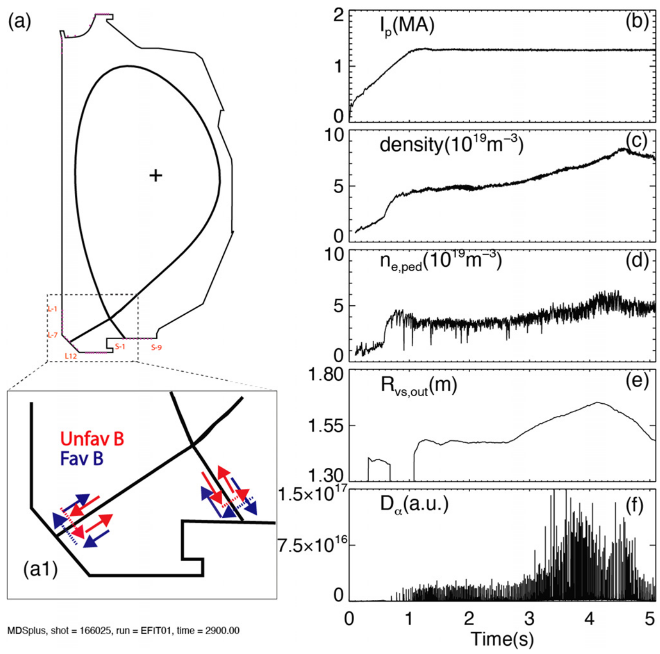

FIG. 1. Left: an example of plasma shape and (a1) schematic plot for the electrical drift flows, red arrows for the unfavorable B_T direction (reversed B_T), and blue arrows for the favorable B_T direction (forward B_T). The second separatrix is outside the vessel and does not affect the physics study in this paper. Right: (b) plasma current, (c) line-averaged density, (d) pedestal density at the pedestal top, (e) outer strike point locations, and (f) $D\alpha$ emission from the outer target plate. The Langmuir probes at the lower inner and outer targets are marked in (a) with the probes L-8 to L12 at the 45° slanted target plate.

sweeping voltage with frequency ~1 kHz was applied to the probes to obtain the I–V characteristics. Then based on the conventional single-probe theory,[15] several plasma parameters, such as the ion saturation current I_{sat}, electron temperature T_e, ground current J_0, and floating potential ϕ_f, are determined from the curve fitting on the I–V characteristics, and some other parameters, i.e., parallel ion current J_{sat} (I_{sat}/A, A is the area), electron density n_e, and parallel heat flux $q_{//}$($q_{//} = \gamma\ J_{sat}\ T_e$, $\gamma = 7$ in this work) are inferred. The plasma space potential ϕ_p is calculated from ϕ_f and T_e by the conventional probe theory,

$$\phi_p = \phi_f + 2.8T_e. \tag{1}$$

Here, the factor of 2.8 is based on the assumptions of $T_i = T_e$ and neglecting the secondary electron emission coefficient δ_e. The radial electric field E_r near the divertor target plate is estimated from the radial gradient of the plasma potential along the horizontal target plate: $E_r = -\nabla_r\ \phi_p$. The poloidal electric drift velocity $v_{E,\theta}$: $v_{E,\theta} = E_r \times B/B^2$. The radial electric drift velocity $v_{E,r}$ from the poloidal electric field E_θ: $v_{E,r} = E_\theta \times B/B^2$. Note that as discussed later, the drift flow could change the flow velocity toward the target plate via coupling with the sheath boundary condition; hence, the calculated density with ion sound speed velocity may not be valid. But, to align with the conventional theories, we will still use sound speed assumption for the density calculations.

Figure 1 shows an example of magnetic configuration of an H-mode discharge used in this paper with plasma current Ip ∼ 1.3 MA, neutral beam injection (NBI) heating ∼5.5 MW, and $B_T \sim 2$ T with ion $B \times \nabla B$ toward the X-point of the open lower single-null divertor configuration. X-point sweeping was used to obtain the divertor target profiles. The continuity of profiles is verified through the sweep by overlapping mapped data from different Langmuir probes. In this discharge, the sweep is about 25 cm which is much wider than the SOL width of ∼4 cm and the probe spacing of ∼2.8 cm. Figure 2 shows the target profiles of the ion saturation current, electron temperature, floating potential, parallel heat flux, and electron density. The profiles are obtained from different probes at different radial locations and the same toroidal location. The probe locations are mapped with the strike point locations based on the EFIT equilibrium reconstruction. The median filter is applied for the data to eliminate ELMs (edge-localized modes) and bad fits. The median filter is considered more appropriate than the smooth or average, since the latter could dilute the weight of the bad points with not well-converged fits and large fit error bars. The profiles are the characteristic of the inter-ELM phase, since the ELM duration is much shorter than the inter-ELM period. Note that the data shown in Fig. 2 are obtained during the strike point sweeping between 3.1 and 4 s with the pedestal density remaining similar to 20% variation throughout this period. The upstream and pedestal electron density and temperature profiles are measured by the Thomson scattering with high temporal and spatial resolution.[16] However, the line-averaged density is increasing during this period. The ELMs during this period are type-I with frequency of about 60–70 Hz. As can be seen, the profiles are well matched with each other. Hence, based on this X-point sweeping technique, more points for radial profiles can be obtained to facilitate the analysis, especially for the calculation of the radial derivative of the plasma potential.

III. DIVERTOR PLASMA PROFILES IN FORWARD B_T PLASMAS

A. Low density plasmas

It is evident that there is a large in–out asymmetry between the inner and outer divertor plasmas with a greater heat flux deposited at the outer divertor target plate than that at the inner divertor target

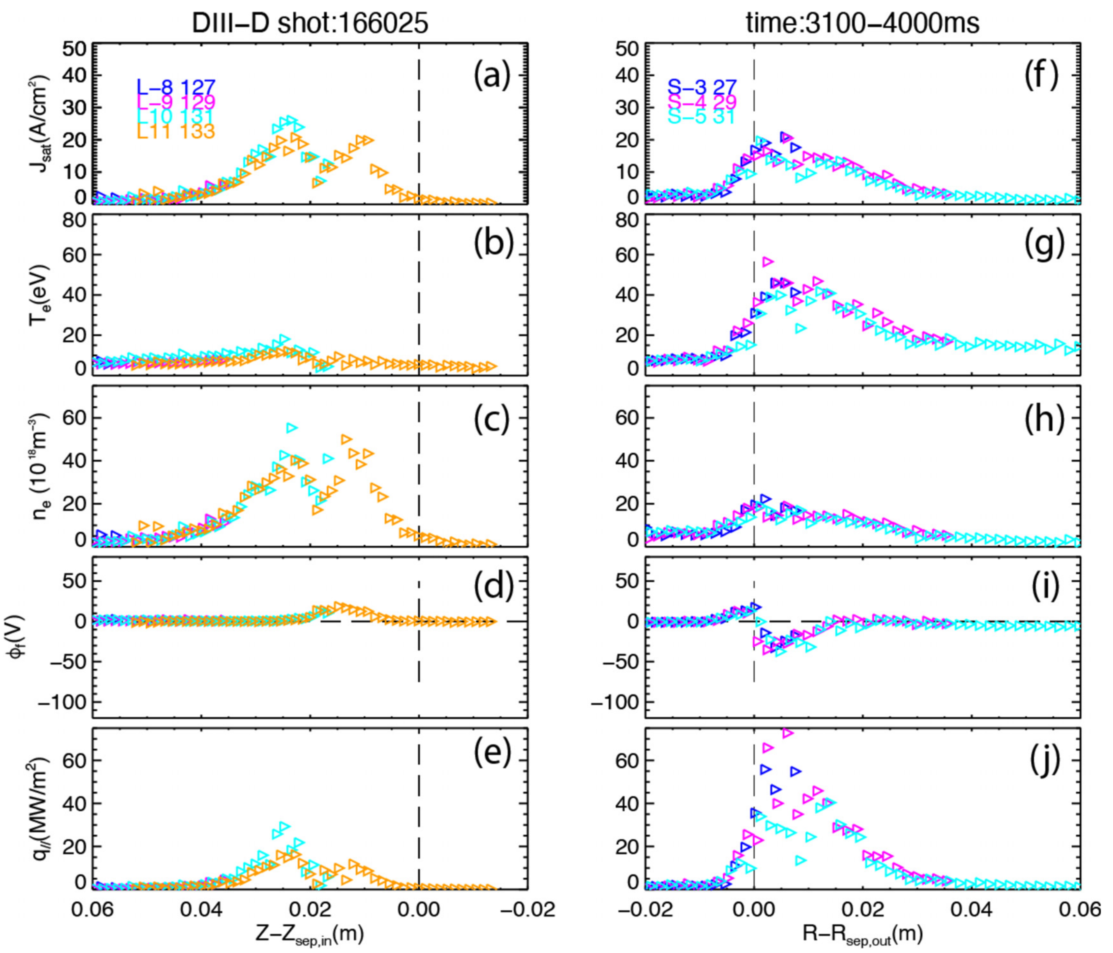

FIG. 2. The target profiles near the inner strike point (left) and the outer strike point (right) for [(a) and (f)] ion saturation current density, mostly in the parallel direction, [(b) and (g)] electron temperature, [(c) and (h)] electron density inferred by assuming sound speed, [(d) and (i)] floating potential, and [(e) and (j)] parallel heat flux calculated by assuming $\gamma = 7$. Low pedestal density case, $n_{e,ped}$ ∼4.0×10^{19} m^{-3}.

plate, as can be seen in Fig. 2. The plasma at the outer strike point is much hotter with the peak T_e about 50 eV, which suggests that the divertor is in the attached condition. However, the temperature at the inner target is significantly lower, with T_e about 5 eV near the inner strike point, suggesting that the inner divertor plasma could be in either high recycling or detached states. The parallel particle flux as indicated by the ion saturation current J_{sat} near the inner strike point is very close to but slightly higher than that near the outer strike point. It is interesting that the particle flux at the inner target exhibits a double-peak structure, and the temperature profile also shows a similar double-peak structure, albeit less pronounced. In particular, the second J_{sat} peak at ∼2 cm away from the separatrix is even higher than the first peak near the separatrix by ∼30% in this discharge. In contrast, the particle flux profile at the outer target only shows a very minor double-peak structure with the dip right near the peak T_e region. T_e and J_{sat} profiles exhibit similar radial decay lengths. It is worth pointing out that this double-peak structure has been observed in many DIII-D discharges and the amplitudes of the double peaks can be at similar levels. Also note that the double peak structure appears on several probes during the strike point sweeping and the profiles could be well matched after mapping to the equilibrium. This indicates that the second peak is not due to the different divertor target geometry, when the inner strike point moves across the probe from the slanted target to the horizontal floor target. The high flux around the inner second peak is also consistent with the so-called high-field-side high-density front observed in ASDEX-Upgrade.[17]

Such a double-peak structure has been found in JET[18] and is also found in boundary modeling with drifts turned on.[6] This double-peak structure is different from the splitting of the strike point due to the internal or external error fields which may connect the field line from the core plasma to the target plate.[19] Typically, the error field could result in a multi-peak structure in the floating potential. However, in this case, the floating potential does not show double-peak structures, implying that such a double-peak structure is not due to the error field. In addition, increasing the plasma density can reduce the first peak near the strike point (as shown later), which also suggests that this double peak structure is more likely due to local divertor plasma conditions.

The radial profile of the floating potential near the inner strike point is significantly different from that near the outer strike point. Across the inner target, the floating potential is always positive with a peak value of about 20 V. However, at the outer target, the floating potential increases from about 0 V in the private flux region to about 20 V near the strike point. Moving a little further outward into the SOL, the floating potential profile then sharply decreases with a larger negative dip (−30 V) near the peak temperature region. Then, moving further outward, the floating potential is increased to a positive value approximately a few Volts in the near SOL and slightly decreased to be below 0 V in the far SOL.

The floating potential could contribute a comparable fraction to the plasma potential as the temperature gradient does. Meanwhile, the large spatial variation of the floating potential at the outer target well correlates with the strong radial variation of the SOL current, as shown in Fig. 3. This implies the important roles of the SOL current on the drift flow and thus the divertor conditions.[20,21] The SOL current can be measured by the Langmuir probe as the so-called ground current.[2] As can be seen in Fig. 3, similar to the floating potential profiles, the SOL current shows similar radial profiles with the same order of magnitude as the parallel ion flux, which suggests a significant imbalance between the electron and ion fluxes in the SOL. The SOL current changes direction around the strike point, which is also consistent with the previous UEDGE modeling.[22] The radial variation of the SOL current has been reported in other tokamaks and explained by several physical mechanisms,[23] such as the thermal-electric current and Pfirsch–Schuluter current. In the SOL region, the thermal–electric current,[24] which arises from the temperature difference between the inner and outer divertors, is thought to be the dominant component. In the private flux region, the Pfirsch–Schuluter current, which mainly resulted from the charge separation from the magnetic drift and diamagnetic drift, could be dominant while the thermal–electric current would be weak.[25] Changing divertor conditions, such as temperature profiles and magnetic drift directions, could strongly change the SOL

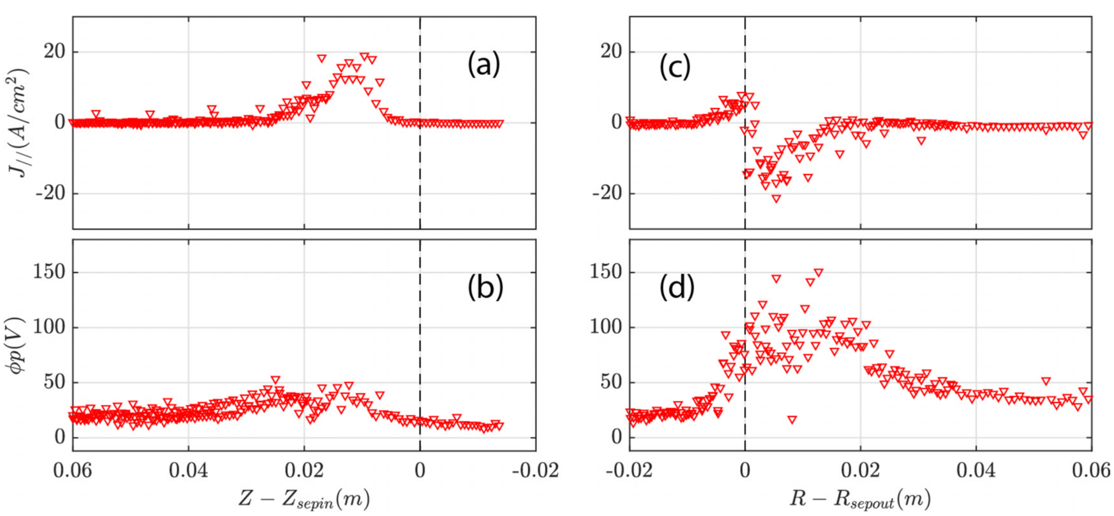

FIG. 3. The target profiles for near the inner strike point (left) and near the outer strike point (right) for [(a) and (c)] ground current and [(b) and (d)] plasma potential.

current and thus drift flows. In turn, the drift flow strongly affects the particle distribution and thus could strongly influence the divertor current.[20]

The radial profile of plasma potential can be determined based on the temperature and floating potential profiles as shown in Fig. 3. The outboard SOL is hotter with much higher T_e, which results in higher plasma potential, while the inboard SOL has lower plasma potential. The plasma potential profile in the outboard SOL peaks near the peak temperature region and exhibits strong gradients near the outer strike point, while in the inboard SOL, the plasma potential profile is much flatter suggesting a near zero radial electric field.

As can be seen in Fig. 4, the outboard radial electric field near the strike point is estimated to be 5 ± 1 kV/m, which results in a poloidal electric drift velocity $v_E \sim 2.5 \pm 0.5$ km/s. As shown in Fig. 1(a1), the poloidal $E_r \times B$ flow moves the particle from the outer divertor to the inner divertor via the private flux region along the poloidal field direction, which may hence cooldown the inboard divertor plasma and reduce the heat flux near the inner strike point. This flow velocity is of the same order of magnitude as the poloidal projection of the parallel ion sound speed, $C_s \sim \sqrt{2T_e/m_i} \sim 70$ km/s. The field line angle is about 3° and thus the inferred perpendicular flow velocity is about 3.6 km/s. The poloidal drift flow velocity is about $70 \pm 14\%$ of the perpendicular plasma flow velocity, implying that the electrical drift could move $70 \pm 14\%$ of particle flux near the strike point from the outer divertor to the inner divertor region. This is consistent with previous measurements,[12] thus suggesting the significant role of the drift on the in–out divertor asymmetry. Note that a negative Er spans from the private flux region to +1 cm in the SOL, suggesting that, in the near SOL, it may drive some plasma flow upstream. This is mainly due to the displacement of the peak temperature profile from the outer strike point, which has been commonly observed in the other dataset. In the far SOL region, E_r is about 3 kV/m with the corresponding $v_E \sim$ 1.5 km/s in a wider region, which tends to drag the plasma flow toward the target plate, although it is smaller than the poloidal projection of sound speed parallel flow velocity. At the high field side, the inferred radial electric field is about 1.0 kV/m near the inner strike point, leading to a poloidal drift of 0.5 km/s, while in the inner divertor far-SOL, the radial electric field drift and the resulting poloidal drift are strongly reduced to nearly zero.

The low temperature in the inner divertor and thus the significant gradient along the field line could result in a poloidal electric field. This is because the poloidal electric field is strongly correlated with the temperature and pressure gradient along the field line: $E_\theta = BJ_{//}/B_\theta\sigma - 0.71\partial T_e/\partial L_\theta - \partial P_e/n_e\partial L_\theta$, where $J_{//}$ is the parallel current, σ is the plasma conductivity, B_θ is the poloidal magnetic field, and L_θ is the poloidal distance. Unfortunately, no upstream potential measurements are available. On the outboard side, based on the upstream profiles measured from the multi-pulse core Thomson scattering system, and using the power balance technique,[26,27] the separatrix temperature is estimated to be 90 eV which is much higher than those near the divertor target, i.e., $T_{e,out} \sim 50$ eV and $T_{e,in} \sim 10$ eV. The averaged poloidal electric field near the outer strike point is about 0.14 kV/m with upstream–downstream temperature difference of about 40 eV, a poloidal leg length of about 0.2 m, and no parallel pressure loss. By using the power balance technique, we could obtain even a similar lower poloidal electric field: $q_\parallel \sim 2\kappa_e\partial T_e^{7/2}/7\partial L_\parallel$, with $q_{//} \sim 60$ MW/m^2, $\kappa_e \sim 2000$, $T_{e,out} \sim 50$ eV, and 3° field line angle, and the poloidal electric field near the outer divertor target plate would be 0.03 kV/m. With this weak poloidal electric field ($\ll$0.3 kV/m), the radial drift flow is weak to push a significant particle flux from SOL toward the strike point. It is consistent with the observation of no strong double peak structure. In contrast, the low T_e and the associated parallel pressure loss in the inner divertor would induce a stronger parallel temperature gradient and poloidal electric field. With $q_{//} \sim 20$ MW/m^2, $T_e \sim 10$eV, 3° field line angle, and weak contribution from density, the poloidal electric field near the divertor target plate would be 1 kV/m ($E_\theta \sim -1.71\partial T_e/\partial L_\theta$), corresponding to a radial flow velocity 0.5 km/s, which is higher than the previous value. There is still a large uncertainty in the amplitude of this flow velocity, but it should be higher than that in outer SOL. The wide flux profiles at the inner target

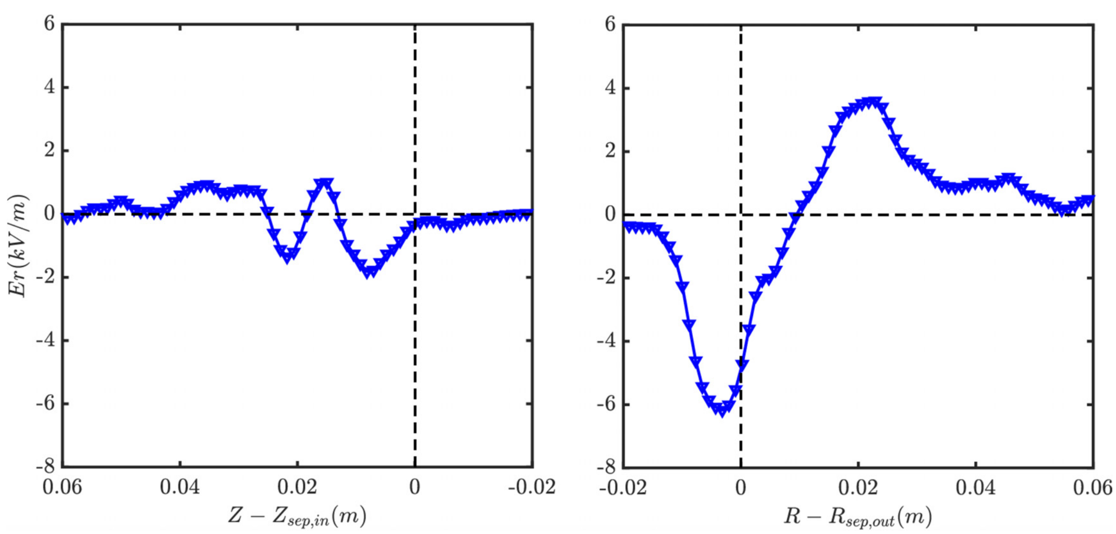

FIG. 4. The Er profiles near the inner strike point (left) and outer strike point, calculated based on the plasma potential profiles in Fig. 3.

qualitatively agree with the physics picture of drift flow. However, the double peak structure requires more quantitative study and dedicated measurements. We will discuss it later.

B. Detachment dynamics with forward B_T

To achieve divertor detachment, gas puffing was used to increase the upstream plasma density, i.e., the separatrix density, and thus decrease the plasma temperature in the divertor region. As we can see in Fig. 5, first, increasing the pedestal density to $n_{e,ped} = 7 \times 10^{19}$ m^{-3} increases the ion saturation current, i.e., particle flux, and reduces electron temperature at the outer strike point. As the density further increases to $n_{e,ped} = 9 \times 10^{19}$ m^{-3}, the outer divertor plasma enters detachment with strong reduction in both J_{sat} and T_e near the outer strike point, as measured by the target Langmuir probes. However, the divertor plasma is still attached in the far-SOL region with the peak J_{sat} shifting outward, about 2 cm away from the strike point and T_e remaining low there. It is interesting to note that at the inner target, as the density increases, the double peaks of J_{sat} first overlap to form a single and large peak that is at a similar level to the peak J_{sat} at the outboard target. Then, as the density further increases, Jsat is significantly reduced, and T_e is further reduced with the T_e peak near the inner strike point greatly diminished. Note that the increasing density would increase the ELM frequency to be 80–100 Hz at $n_{e,ped} = 7 \times 10^{19}$ m^{-3} or ∼120 Hz. The ELMs remain type-I regime, and the power across separatrix P_{SOL} is only reduced by 0.2 MW at the highest density case.

Figure 5 compares the target profiles of floating potential, ground current, and plasma potential at two different pedestal densities. As can be seen, compared to Fig. 3, as density increases, the floating potential and ground current are strongly reduced at both outer and

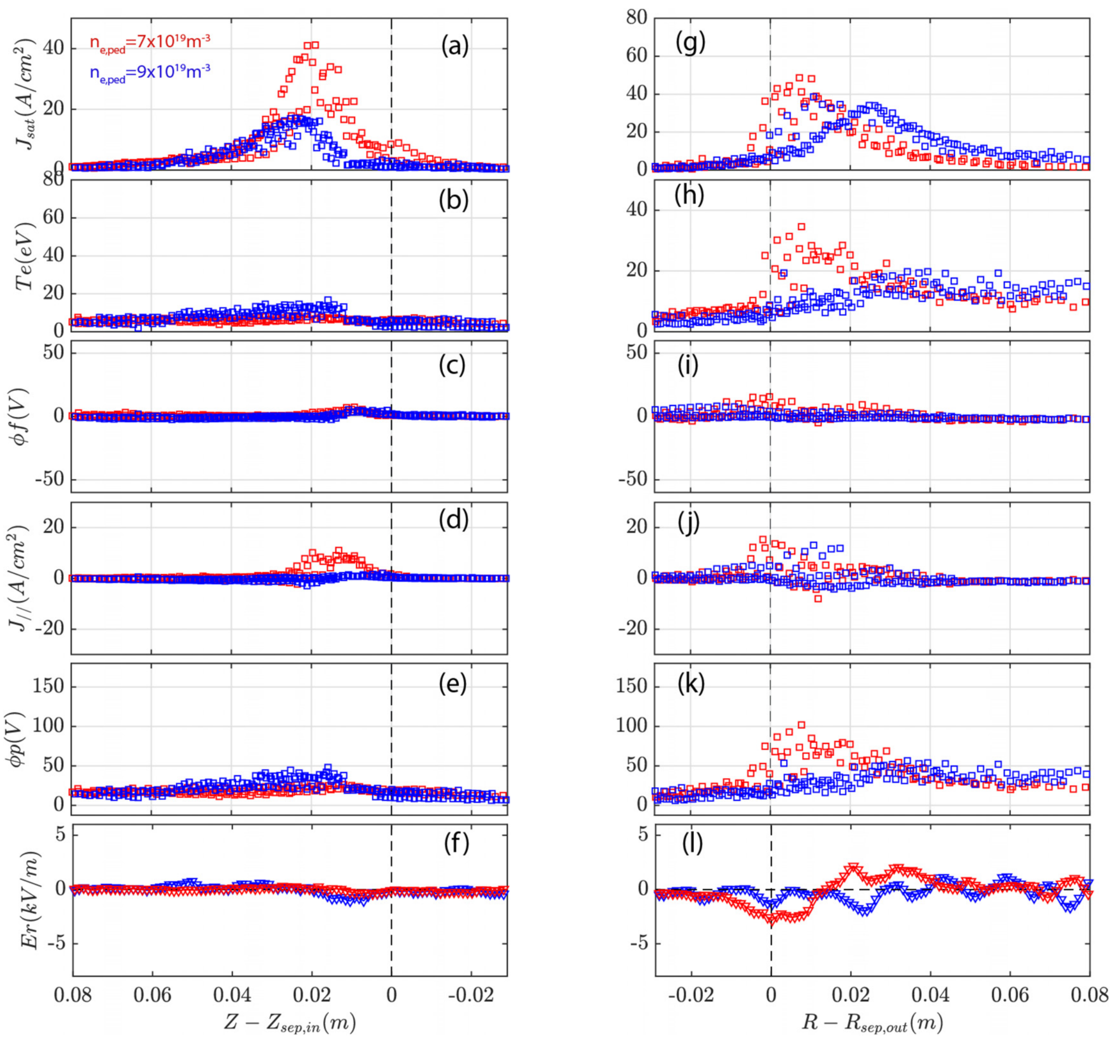

FIG. 5. The target profiles at the inner (left) and outer (right) divertor targets: [(a) and (g)] ion saturation current, [(b) and (h)] electron temperature, [(c) and (i)] floating potential, [(d) and (j)] ground current, [(e) and (k)] plasma potential, and [(f) and (l)] Er profiles at two pedestal densities, 7.0×10^{19} m^{-3} (red) and 9×10^{19} m^{-3} (blue), the same plasma configuration as that in Figs. 2–4.

inner targets, which correlate with reduced T_e. It is interesting to note that once the outboard SOL detaches, both the floating potential and the temperature are strongly reduced, with nearly flat profiles. Hence, as can be seen in Figs. 5(f) and 5(l), the inferred plasma radial electric field is reduced to nearly zero at detachment so that the poloidal drift would be diminished too. The weak poloidal drift would not contribute to a significant particle flow near the target plate, in particular, from the outer divertor to the inner divertor, although the drifts and associated flows may still exist upstream of the target and result in some particle flows toward the inner divertor.

IV. DIVERTOR PLASMA PROFILES IN REVERSED B_T PLASMAS

A. H-mode plasmas with density scan

When the magnetic field direction is reversed, the in–out divertor asymmetry was found to be strongly reduced. Another notable difference for reversed B_T is that the double-peak structure clearly seen on the ion saturation current profile appears at the outer divertor target (Fig. 6), similar to that observed at the inner target for forward B_T. Figure 6 shows two discharges with reversed B_T at two different densities. Note that the plasma conditions of Fig. 6 are different from that in Figs. 2–5, although the magnetic configuration is similar. These two discharges were run at Ip ∼ 1 MA, 4 MW NBI heating, different densities but both type-I ELM H-mode plasmas. The divertor conditions were changed from high temperature state to low temperature, which is beneficial for the comparison. Note that the similar observations are made across different plasma conditions.

As shown in Fig. 6, the particle flux profile near the outer divertor is much broader than the temperature profile. The temperature profile exhibits a single peak, well aligned with the first peak of J_{sat} located near the outer strike point at low density. Near the inner strike point, only a single J_{sat} peak is observed, and the temperature is still much lower than that near the outer strike point. The difference in the in–out target profiles between the forward and reverse B_T strongly suggests the important impact of the drift and flows that depend on the field direction.

Another dramatic difference is observed on the floating potential profiles, Figs. 6(c) and 6(i), as well as the ground current profiles, as can be seen in Figs. 6(d) and 6(j). At the inner divertor plate, the floating potential shows a positive–negative variation approaching the inner strike point, while only positive floating potential is present near the target for forward B_T. At the outer divertor target, the floating potential in the private flux region becomes flat and negative, in contrast to the peaked positive potential for the forward B_T direction. Further, the floating potential turns sharply into a more negative dip across the separatrix for reverse B_T, while a sharp transition from positive to negative occurs across the outer strike point for the forward B_T case. The location of this turning point appears to agree well with the EFIT strike point location.

In the private flux region of the outer divertor, the negative floating potential reduces the plasma potential and thus the radial electric field, especially as the temperature near the outer strike point is reduced at high density. In other areas, the plasma potential profile is similar to that in the forward B_T, suggesting a similar radial electric field. With the B_T reversal, the radial electric flow is also reversed. The poloidal flow moves the particles from the inner divertor through the private flux region toward the outer divertor, which would facilitate detachment near the outer strike point. The radial drift moves the particles from the inboard SOL toward the private flux region, thus enhancing the polodial drift toward the outer strike point. In the outboard SOL, the poloidal drift moves the particles away from the target plate, which may reduce the degree of detachment near the target plate, while the radial drift moves the particles toward the outer SOL region.

Increasing the density reduces the temperature near the outer strike point. As the pedestal density increases from 3.7×10^{19} m^{-3} to 5×10^{19} m^{-3}, the temperature is reduced and flattened across a wide region. For the high density case, T_e near the outboard divertor target plate measured from divertor TS is about 2 eV, indicating divertor detachment. This is consistent with the flat temperature profiles, although probes show a higher T_e of about 10 eV. The discrepancy of T_e under this B_T direction may be related to the kinetic effects[2,28] or temperature gradient[29,30] or plasma resistance[31] but is still an open question. The first peak (closer to the outer strike point) of particle flux moves closer to the strike point and is much narrower. The first peak looks to be merged with the large second peak. As aforementioned, the profile of J_{sat} features a double-peak structure, with first J_{sat} peak, closer to the strike point, appearing at the same location as the T_e peak. In particular, at high density, J_{sat} peaks at ∼2 cm away the strike point. Increasing the pedestal density reduces the temperature by 50%, and the peak particle flux increases by ∼50%; thus, the peak heat flux at the divertor target $q_\perp \sim J_{sat}T_e$ is only reduced slightly and plasma momentum loss is very small, in spite of a significant increase in density. This shows that it is more difficult to achieve effective divertor detachment (i.e., reducing both peak $q_\perp$ and peak T_e) at the outer target for the reverse B_T case for the open divertor configuration investigated here. This is consistent with the observation in Refs. 32 and 33. The main reason is due to the drift-induced separation of particle flux and peak temperature that reduces the cooling effect of recycling neutrals.

B. Correlation of double peak structure with power and density in L-mode plasmas

The double peak structure can also be found in the L-mode plasmas under reversed B_T conditions, as shown in Figs. 7 and 8 for a density and power scan, respectively. The plasma shape and current are similar to that shown in Fig. 6, but with much less power. No neutral beam power is added in these shots, although some small beam blips are applied for the diagnostics. The dynamics of the double peak structure and divertor plasma profiles are similar to those observed in the H-mode plasmas. At low density, the divertor temperature profiles are broad with high T_e peaked near the SOL, and the density profiles exhibit a double peak structure with the second peak of about 10 cm away the outer strike point. Increasing the density increases the entire particle flux profile and narrows the temperature profile toward the strike point with a reduced peak. The first peak in the density profile aligns with temperature peak and the second peak is shifted closer to the first peak. In particular, at the highest density, the temperature profile is close to flat such that the first peak is very narrow and the two peaks look to be merged to form a large peak. This is similar to that in the H-mode plasmas, implying similar underlying physics. Another interesting finding is that the dip between the two peaks is near the steep gradient region of temperature and plasma potential and moves along with the temperature profile. Near the dip, the

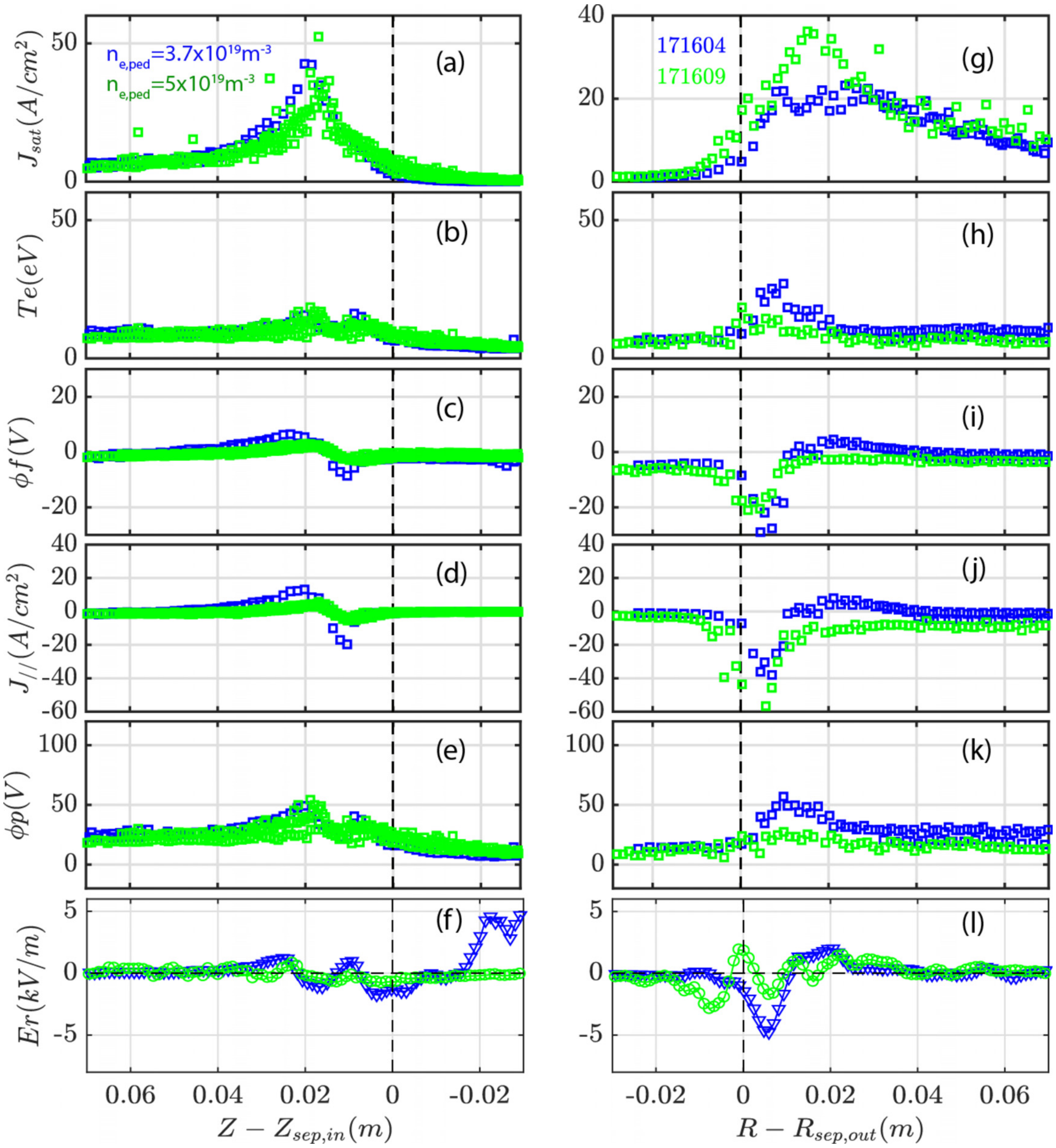

FIG. 6. The target profiles at the inner (left) and the outer (right) divertor targets: [(a) and (g)] ion saturation current, [(b) and (h)] electron temperature, [(c) and (i)] floating potential, [(d) and (j)] ground current, [(e) and (k)] plasma potential, and [(f) and (l)] radial electric field at two pedestal densities $n_{e,ped} = 3.7 \times 10^{19}$ m^{-3} (red) and 5×10^{19} m^{-3} (blue) in reversed B_T H-mode plasmas.

electron temperature remains high, i.e., about 30 eV (half of the peak T_e) for both the low density and middle density cases.

The power scan exhibits similar behavior as the density scan. Increasing the heating power broadens the temperature and plasma potential profiles. The double peak in the density profile is also broadened and shifted outward. The double peak structure moves along with the temperature profile. It is interesting to find that at the highest power, the density and particle flux remain high even at >15 cm outside of the strike point. This wide SOL profile may challenge future divertor designs, since the neutral and recycling flux are not easily confined by an open divertor.

C. Physics of the double peak structure

The presence of the double peak structure and dependence on the B_T direction confirm the physical discussion in Ref. 3, which highlights the role of the drift flow on divertor plasma profiles. As discussed in Ref. 3, the double peak structure is mainly due to the

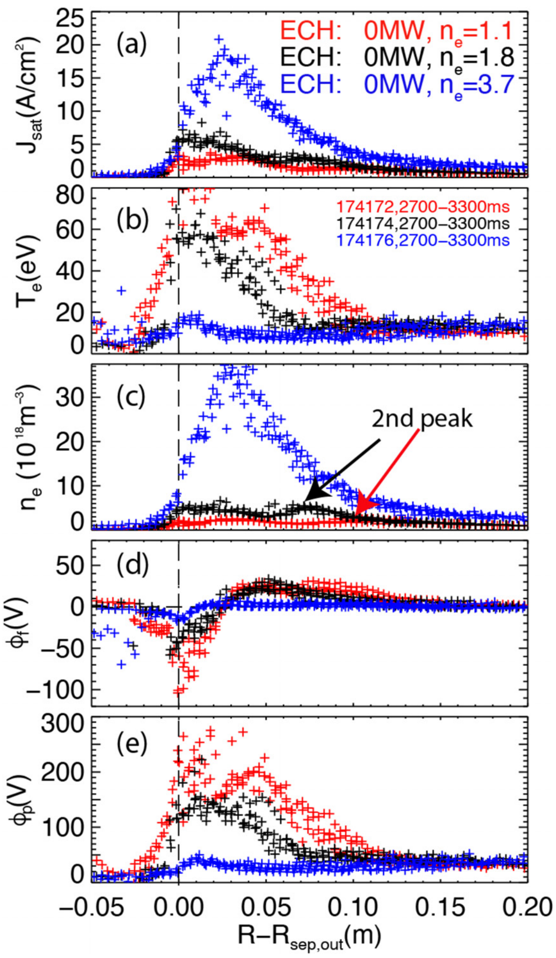

FIG. 7. The radial profiles of (a) J_{sat}, (b) T_e, (c) electron density, (d) floating potential, and (e) plasma potential at the outer divertor target for reversed B_T L-mode plasmas with low line-averaged density $n_e \sim 1.1 \times 10^{19}\ m^{-3}$ (red), middle density $n_e \sim 1.8 \times 10^{19}\ m^{-3}$ (black), and high density $n_e \sim 3.7 \times 10^{19}\ m^{-3}$ (blue). Only Ohmic heating, and no ECH and NBI.

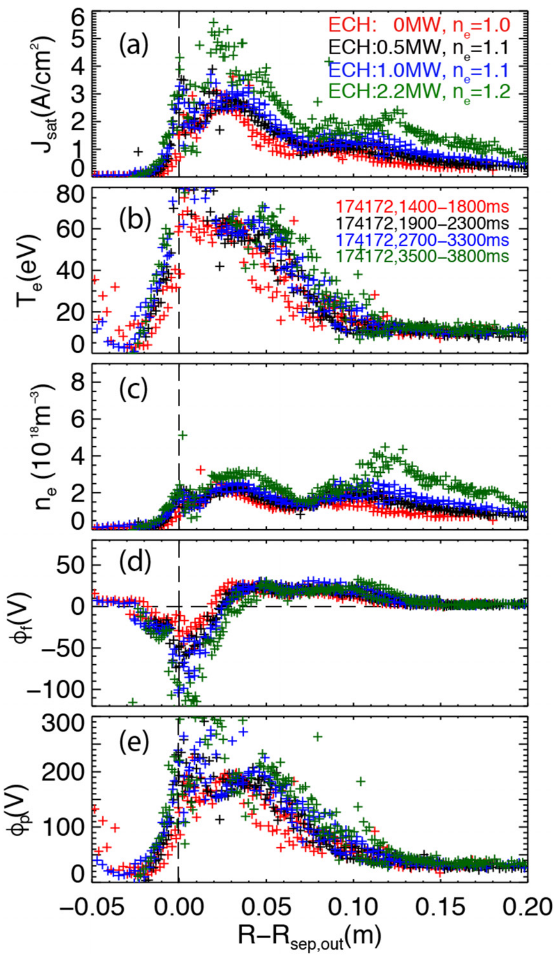

FIG. 8. The radial profiles of (a) J_{sat}, (b) T_e, (c) electron density, (d) floating potential, and (e) plasma potential at the outer divertor target for reversed B_T L-mode plasmas with nearly same density but different heating powers: Ohmic-only heating (red), ECH power ~0.5 MW (black), ECH power ~1 MW (blue), and ECH power of about 2.2 MW (green).

contribution of drift flows from both the poloidal and radial components. The detailed physics analysis requires dedicated divertor Thomson scattering measurement. In this paper, we will just briefly introduce the critical physics idea.

The first peak of the density and particle flux in the outer SOL with reversed B_T aligns with the peak temperature region corresponding to the main heat flux deposition. The parallel temperature gradient can induce a significant poloidal (or parallel) electric field and associated radial $E \times B$ flow that moves the particles toward the far SOL. The amplitude of the radial drift flow decays significantly radially due to the temperature radial decay.

The second peak of density and particle flux profiles is mainly due to a strong poloidal electric field around the density dip. This poloidal electric field is mainly due to the poloidal density gradient and static pressure loss. This originates from the coupling of the sheath boundary condition with the poloidal drift flow, as discussed below. The strong temperature gradient leads to a significant radial electric field and thus drift flow. The positive radial electric field drives the poloidal flow away from the target plate at a flow velocity which is nearly of the same order as the poloidal projection of the ion sound speed, $V_{E_r \times B} \sim -C_s B_\theta / B$. Based on the modified Bohm–Chrodura boundary condition at the entrance of magnetic pre-sheath,[34]

$$\frac{B_\theta}{B} v_{//i} + \frac{E_r}{B} = \frac{B_\theta}{B} C_s. \tag{2}$$

The electrical drift flow which is away from the divertor target plate would lead to a supersonic parallel ion flow $V_{//i}$ with Mach number of about 2. Physically, the radial electric field could accelerate the plasma flow to supersonic by an increment of E_r/B_θ. From the Mach probe measurements in several tokamaks including JET,[35] ASDEX-Upgrade,[36] JT-60U,[37] and DIII-D,[38] the typical Mach number in the outer-midplane SOL is about 0.2–0.5. Taking these numbers into the parallel pressure balance equation between the upstream and downstream,[2]

$$\left(p_e + p_i + m_i n_i v_{//i}^2\right)_t = \left(p_e + p_i + m_i n_i v_{//i}^2\right)_u. \quad (3)$$

The static electron pressure and the density near the target are both much smaller than that of the upstream, both of which quantitatively agrees with the experimental observations.

Such a pressure loss does not require strong momentum dissipation from neutrals, which agrees with the fact that the double peak structure only happens in attached plasma conditions. In addition, the momentum dissipation by recycling neutrals requires low plasma temperature, i.e., $T_e < 10$ eV.[39,40] As can be seen in Figs. 7 and 8, around the density dip, the electron temperature is well above 10 eV, suggesting less importance of neutrals for the pressure loss. This physics picture is consistent with previous theoretical prediction.[41]

The drift flows play important roles in the particle transport and thus forming the double peak structure in flux and density profiles. However, such a double peak structure is not clear in the temperature profiles. This is also consistent with the picture that the thermal transport is dominated by the heat conduction rather than convection in the high temperature divertor.[42]

The physics of inner divertor double peak structure in forward B_T plasmas is still unclear. The temperature is low and the associated radial electric drift flow is weak. Thus, the poloidal projection of parallel flow and poloidal electrical drift flow may be still comparable and eventually lead to the double peak structure. As a result of the low temperature, another physical mechanism[10] may take over. Based on the previous EDGE2D simulation, the divergence of the radial $E \times B$ could result in another kind of doubly peak structure. The poloidal drift flow moves particles from the outer divertor toward the inner divertor that leads to a partial detached divertor and strong poloidal electric field. While, in the far SOL, temperature and flux remain high, which causes an inversion of the poloidal electric field. In addition, the SOL current due to the in–out asymmetry is also reversed in the inner SOL, which also contributes partly to the inversion of poloidal electric field. The inversion of the poloidal electric field and associated radial flow could eventually result in the double peak structure. Furthermore, the divertor geometry in the HFS is more closed than the outer divertor, which may affect the inner divertor behavior as well. Further physics study requires detailed and accurate plasma profile measurements which are not routinely available presently.

V. SUMMARY

With the direct measurement of the ground current, floating potential and temperature from target Langmuir probes, the plasma potential, radial electric field, and resulting poloidal drift are inferred to understand the effect of drifts on the divertor plasmas in H-mode and L-mode conditions in DIII-D with an open lower single-null divertor configuration. In forward B_T attached plasmas, the poloidal drift moves the particle from the outer divertor region via the private flux region toward the inner strike point, which facilitates the cooling down of the inboard divertor and thus enhances the radial drift due to the gradient between upstream and downstream conditions. This may contribute to the appearance of a double-peaked structure at the inner target and may also partly explain the in–out asymmetry. As the upstream plasma density increases, the double-peak structure becomes a single peak, which may result from the decrease in the poloidal drift and enhanced radial drift. Reversing the B_T direction reverses both poloidal and radial electric drifts. This appears to facilitate the cooling of the outer strike point and divertor detachment. However, the particle flux profile becomes much broader with a double-peak structure similar to the inner target profile with forward B_T, presumably due to the enhanced radial drift which pushes particles toward outboard SOL. Furthermore, the particle flux and thus the momentum remain high near the outer strike point, and hence the peak heat flux at the outer divertor target is not effectively reduced, compared with the forward B_T. The correlation of double peak structure with divertor temperature profiles and drifts under reversed B_T can be well explained by the coupling between the drift flow and sheath boundary condition. This also highlights the important role of drifts on the global particle and power balance, which should be considered for future divertor design.

ACKNOWLEDGMENTS

This work is supported by the U.S. Department of Energy under Nos. DE-FC02–04ER54698, DE-AC05–06OR23100, and DE-AC04–94AL85000 and General Atomics Postdoctoral Research Participation Program administered by ORAU.

This report was prepared as an account of work sponsored by an agency of the United States Government. Neither the United States Government nor any agency thereof, nor any of their employees, makes any warranty, express or implied, or assumes any legal liability or responsibility for the accuracy, completeness, or usefulness of any information, apparatus, product, or process disclosed, or represents that its use would not infringe privately owned rights. Reference herein to any specific commercial product, process, or service by trade name, trademark, manufacturer, or otherwise, does not necessarily constitute or imply its endorsement, recommendation, or favoring by the United States Government or any agency thereof. The views and opinions of authors expressed herein do not necessarily state or reflect those of the United States Government or any agency thereof.

DATA AVAILABILITY

Raw data were generated at the DIII-D facility. Derived data that support the plots within this paper and other findings of this study are available from the corresponding author upon reasonable request.

REFERENCES

[1]A. Loarte, B. Lipschultz, A. S. Kukushkin, G. F. Matthews, P. C. Stangeby, N. Asakura, G. F. Counsell, G. Federici, A. Kallenbach, K. Krieger, A. Mahdavi, V. Philipps, D. Reiter, J. Roth, J. Strachan, D. Whyte, R. Doerner, T. Eich, W. Fundamenski, A. Herrmann, M. Fenstermacher, P. Ghendrih, M. Groth, A. Kirschner, S. Konoshima, B. LaBombard, P. Lang, A. W. Leonard, P. Monier-Garbet, R. Neu, H. Pacher, B. Pegourie, R. A. Pitts, S. Takamura, J. Terry, E. Tsitrone, I. S. Layer, and D.P.T. Group, Nucl. Fusion **47**, S203 (2007).

[2]P. C. Stangeby, *The Plasma Boundary of Magnetic Fusion Devices* (IOP Publishing, Bristol, 2000).

[3]H. Q. Wang, H. Y. Guo, G. S. Xu, A. W. Leonard, X. Q. Wu, M. Groth, A. E. Jaervinen, J. G. Watkins, T. H. Osborne, D. M. Thomas, D. Eldon, P. C. Stangeby, F. Turco, J. C. Xu, L. Wang, Y. F. Wang, and J. B. Liu, Phys. Rev. Lett. **124**, 195002 (2020).

[4]B. LaBombard, J. A. Goetz, C. Kurz, D. Jablonski, B. Lipschultz, G. M. McCracken, A. Niemczewski, R. L. Boivin, F. Bombarda, C. Christensen, S. Fairfax, C. Fiore, D. T. Garnier, M. A. Graf, S. N. Golovato, R. S. Granetz, M. J. Greenwald, S. F. Horne, A. E. Hubbard, I. H. Hutchinson, J. H. Irby, J. Kesner, T. Luke, E. S. Marmar, M. J. May, P. O'Shea, M. Porkolab, J. Reardon, J. E.

Rice, J. Schachter, J. A. Snipes, P. C. Stek, Y. Takase, J. L. Terry, G. Tinios, R. L. Watterson, B. Welch, and S. M. Wolfe, Phys. Plasmas **2**, 2242 (1995).
[5]E. T. Meier, R. J. Goldston, E. G. Kaveeva, M. A. Makowski, S. Mordijck, V. A. Rozhansky, I. Y. Senichenkov, and S. P. Voskoboynikov, Plasma Phys. Controlled Fusion **58**, 125012 (2016).
[6]A. V. Chankin, G. Corrigan, M. Groth, P. C. Stangeby, and J. E. T. contributors, Plasma Phys. Controlled Fusion **57**, 095002 (2015).
[7]M. J. Schaffer, B. D. Bray, J. A. Boedo, T. N. Carlstrom, R. J. Colchin, C. L. Hsieh, R. A. Moyer, G. D. Porter, T. D. Rognlien, and J. G. Watkins, Phys. Plasmas **8**, 2118 (2001).
[8]J. A. Boedo, M. J. Schaffer, R. Maingi, and C. J. Lasnier, Phys. Plasmas **7**, 1075 (2000).
[9]T. Eich, B. Sieglin, A. Scarabosio, W. Fundamenski, R. J. Goldston, and A. Herrmann, Phys. Rev. Lett. **107**, 215001 (2011).
[10]A. V. Chankin, G. Corrigan, S. K. Erents, G. F. Matthews, J. Spence, and P. C. Stangeby, Plasma Phys. Controlled Fusion **43**, 299 (2001).
[11]N. Fedorczak, J. Gaspar, Y. Corre, A. Grosjean, X. Courtois, J. P. Gunn, R. Mitteau, R. Dejarnac, J. Bucalossi, E. Tsitrone, T. Loarer, and S. Brezinsek, Nucl. Mater. Energy **27**, 100961 (2021).
[12]H. Reimerdes, G. P. Canal, B. P. Duval, B. Labit, T. Lunt, W. A. J. Vijvers, S. Coda, G. D. Temmerman, T. W. Morgan, F. Nespoli, B. Tal, and TCV Team, Plasma Phys. Controlled Fusion **55**, 124027 (2013).
[13]S. Potzel, M. Wischmeier, M. Bernert, R. Dux, H. W. Müller, A. Scarabosio, and A.U. Team, Nucl. Fusion **54**, 013001 (2014).
[14]J. G. Watkins, D. Taussig, R. L. Boivin, M. A. Mahdavi, and R. E. Nygren, Rev. Sci. Instrum. **79**, 10F125 (2008).
[15]G. F. Matthews, Plasma Phys. Controlled Fusion **36**, 1595 (1994).
[16]D. Eldon, B. D. Bray, T. M. Deterly, C. Liu, M. Watkins, R. J. Groebner, A. W. Leonard, T. H. Osborne, P. B. Snyder, R. L. Boivin, and G. R. Tynan, Rev. Sci. Instrum. **83**, 10E343 (2012).
[17]F. Reimold, M. Wischmeier, S. Potzel, L. Guimarais, D. Reiter, M. Bernert, M. Dunne, and T. Lunt, Nucl. Mater. Energy **12**, 193 (2017).
[18]A. Loarte, R. D. Monk, J. R. Martín-Solís, D. J. Campbell, A. V. Chankin, S. Clement, S. J. Davies, J. Ehrenberg, S. K. Erents, H. Y. Guo, P. J. Harbour, L. D. Horton, L. C. Ingesson, H. Jäckel, J. Lingertat, C. G. Lowry, C. F. Maggi, G. F. Matthews, K. McCormick, D. P. O'Brien, R. Reichle, G. Saibene, R. J. Smith, M. F. Stamp, D. Stork, and G. C. Vlases, Nucl. Fusion **38**, 331 (1998).
[19]J. G. Watkins, T. E. Evans, M. Jakubowski, R. A. Moyer, O. Schmitz, A. Wingen, M. E. Fenstermacher, I. Joseph, C. J. Lasnier, and D. L. Rudakov, J. Nucl. Mater. **390–391**, 839 (2009).
[20]E. T. Meier, R. J. Goldston, E. G. Kaveeva, M. A. Makowski, S. Mordijck, V. A. Rozhansky, I. Y. Senichenkov, and S. P. Voskoboynikov, Nucl. Mater. Energy **12**, 973 (2017).
[21]M. Knolker, T. E. Evans, A. Wingen, A. Bortolon, F. M. Laggner, R. A. Moyer, R. Nazikian, and H. Zohm, Nucl. Fusion **59**, 126020 (2019).
[22]T. D. Rognlien, D. D. Ryutov, N. Mattor, and G. D. Porter, Phys. Plasmas **6**, 1851 (1999).
[23]C. G. Silva, S. J. Fielding, K. B. Axon, and M. G. Booth, J. Nucl. Mater. **266–269**, 679 (1999).
[24]G. M. Staebler and F. L. Hinton, Nucl. Fusion **29**, 1820 (1989).
[25]M. J. Schaffer, A. V. Chankin, H. Y. Guo, G. F. Matthews, and R. Monk, Nucl. Fusion **37**, 83 (1997).
[26]P. C. Stangeby, J. M. Canik, J. D. Elder, C. J. Lasnier, A. W. Leonard, D. Eldon, M. A. Makowski, T. H. Osborne, and B. A. Grierson, Nucl. Fusion **55**, 093014 (2015).
[27]A. W. Leonard, A. G. McLean, M. A. Makowski, and P. C. Stangeby, Nucl. Fusion **57**, 086033 (2017).
[28]O. V. Batishchev, S. I. Krasheninnikov, P. J. Catto, A. A. Batishcheva, D. J. Sigmar, X. Q. Xu, J. A. Byers, T. D. Rognlien, R. H. Cohen, M. M. Shoucri, and I. P. Shkarofskii, Phys. Plasmas **4**, 1672 (1997).
[29]J. Horacek, R. A. Pitts, P. C. Stangeby, O. Batishchev, and A. Loarte, J. Nucl. Mater. **313–316**, 931 (2003).
[30]J. A. Wesson, Plasma Phys. Controlled Fusion **37**, 1459 (1995).
[31]N. Ohno, N. Tanaka, N. Ezumi, D. Nishijima, and S. Takamura, Contrib. Plasma Phys. **41**, 473 (2001).
[32]A. E. Jaervinen, S. L. Allen, D. Eldon, M. E. Fenstermacher, M. Groth, D. N. Hill, C. J. Lasnier, A. W. Leonard, A. G. McLean, G. D. Porter, T. D. Rognlien, C. M. Samuell, H. Q. Wang, and J. G. Watkins, Nucl. Mater. Energy **19**, 230 (2019).
[33]H. Y. Guo, H. Q. Wang, J. G. Watkins, L. Casali, B. Covele, A. L. Moser, T. Osborne, C. M. Samuell, M. W. Shafer, P. C. Stangeby, D. M. Thomas, J. Boedo, R. J. Buttery, R. Groebner, D. N. Hill, L. Holland, A. W. Hyatt, A. E. Jaervinen, A. Kellman, L. L. Lao, C. J. Lasnier, A. W. Leonard, C. Murphy, J. Ren, C. F. Sang, A. C. Sontag, and T. S. Taylor, Nucl. Fusion **59**, 086054 (2019).
[34]P. C. Stangeby and A. V. Chankin, Phys. Plasmas **2**, 707 (1995).
[35]S. K. Erents, R. A. Pitts, W. Fundamenski, J. P. Gunn, and G. F. Matthews, Plasma Phys. Controlled Fusion **46**, 1757 (2004).
[36]M. Tsalas, A. Herrmann, A. Kallenbach, H. W. Müller, J. Neuhauser, V. Rohde, N. Tsois, M. Wischmeier, and ASDEX Upgrade Team, Plasma Phys. Controlled Fusion **49**, 857 (2007).
[37]N. Asakura, S. Sakurai, M. Shimada, Y. Koide, N. Hosogane, and K. Itami, Phys. Rev. Lett. **84**, 3093 (2000).
[38]J. A. Boedo, G. D. Porter, M. J. Schaffer, R. Lehmer, R. A. Moyer, J. G. Watkins, T. E. Evans, C. J. Lasnier, A. W. Leonard, and S. L. Allen, Phys. Plasmas **5**, 4305 (1998).
[39]A. W. Leonard, Plasma Phys. Controlled Fusion **60**, 044001 (2018).
[40]P. C. Stangeby, Plasma Phys. Controlled Fusion **60**, 044022 (2018).
[41]S. I. Krasheninnikov, D. J. Sigmar, and P. N. Yushmanov, Phys. Plasmas **2**, 1972 (1995).
[42]A. Leonard, M. Mahdavi, S. Allen, N. Brooks, M. Fenstermacher, D. Hill, C. Lasnier, R. Maingi, G. Porter, T. Petrie, J. Watkins, and W. West, Phys. Rev. Lett. **78**, 4769 (1997).